Available online at www.sciencedirect.com
ScienceDirect
Biochimica et Biophysica Acta 1758 (2006) 900–907
BIOCHIMICA ET BIOPHYSICA ACTA
BBA
www.elsevier.com/locate/bbamem

A Fourier transform infrared microspectroscopic imaging investigation into an animal model exhibiting glioblastoma multiforme

K.R. Bambery [a,1], E. Schültke [b,c,1], B.R. Wood [a,*], S.T. Rigley MacDonald [b], K. Ataelmannan [c], R.W. Griebel [c], B.H.J. Juurlink [b], D. McNaughton [a]

[a] *Centre for Biospectroscopy, School of Chemistry, Monash University, Melbourne, Victoria 3800, Australia*
[b] *Department of Anatomy and Cell Biology, University of Saskatchewan, Saskatoon, SK, Canada*
[c] *Division of Neurosurgery, University of Saskatchewan, Saskatoon, SK, Canada*

Received 9 January 2006; received in revised form 3 April 2006; accepted 1 May 2006
Available online 17 May 2006

Abstract

Glioblastoma multiforme (GBM) is a highly malignant human brain tumour for which no cure is available at present. Numerous clinical studies as well as animal experiments are under way with the goal being to understand tumour biology and develop potential therapeutic approaches. C6 cell glioma in the adult rat is a frequently used and well accepted animal model for the malignant human glial tumour. By combining standard analytical methods such as histology and immunohistochemistry with Fourier Transform Infrared (FTIR) microspectroscopic imaging and multivariate statistical approaches, we are developing a novel approach to tumour diagnosis which allows us to obtain information about the structure and composition of tumour tissues that could not be obtained easily with either method alone. We have used a "Stingray" FTIR imaging spectrometer to analyse and compare the compositions of coronal brain tissue sections of a tumour-bearing animal and those from a healthy animal. We have found that the tumour tissue has a characteristic chemical signature, which distinguishes it from tumour-free brain tissue. The physical-chemical differences, determined by image and spectral comparison are consistent with changes in total protein absorbance, phosphodiester absorbance and physical dispersive artefacts. The results indicate that FTIR imaging analysis could become a valuable analytic method in brain tumour research and possibly in the diagnosis of human brain tumours.

Keywords: Animal model; Brain tumour; Focal plane array detector (FPA); Fourier transform infrared (FTIR) micro-spectroscopy

1. Introduction

Fourier transform infrared (FTIR) spectroscopy has been applied to numerous cell and tissue samples, however, the technique is still primarily a research tool and direct clinical applications are few. With the advent of multi-array detectors and sophisticated data analytical techniques including multivariate methods and neural networks this situation is bound to change. Recent advances in focal plane array technology have provided a powerful multi-channel infrared detector, which when coupled with a rapid scan FTIR instrument and its multiplexing advantage, enables the simultaneous, fast acquisition of a high number of spectra at essentially diffraction limited spatial resolution. Each spectrum can be correlated to a particular *x*–*y* coordinate and for tissue samples this provides a powerful molecular imaging tool for pathology. The images can be presented in various ways with the simplest way being chemical images where the intensity, or relative intensity of bands associated with macro-molecular components provides the contrast in false colour maps. Cluster analysis, and in particular unsupervised hierarchical cluster analysis (UHCA) can be used to group similar spectra (i.e. regions with similar macromolecular chemistry) into groups or clusters. The resulting false-colour maps generated from cluster analysis or chemical imaging can be directly compared to stained sections to assist in identifying both anatomical and histopathological features at the molecular level.

* Corresponding author.
E-mail address: bayden.wood@sci.monash.edu.au (B.R. Wood).
[1] Contributed equally to the work here presented.

0005-2736/$ - see front matter © 2006 Elsevier B.V. All rights reserved.
doi:10.1016/j.bbamem.2006.05.004

A number of studies have utilised FTIR spectroscopy and chemometric based analysis for tumour detection and classification of tissue samples including cervical [1–5], oral mucosa [6,7], skin [8,9], lymph [10,11], prostrate [12,13], colon [14–16], lung [17], and breast [18,19]. Fewer studies have focussed on brain tissue, with some notable exceptions being investigations of multiple sclerosis plaques [20,21] and scrapie infections of the central nervous system [22,23]. More recently a study utilised FTIR imaging and chemometrics to diagnose astrocytic glioblastoma tissue in human brain sections and demonstrated a 64% classification success rate when various chemometric models were combined to provide an aggregated prediction model [24]. Raman micro-spectroscopy has also been applied to investigate water content [25] and radiation damage in brain tissue [26] but the time required to build maps from Raman measurements renders this technique unsuitable for clinical analysis at present.

C6 cell glioma is a frequently used animal model for glioblastoma multiforme (GBM), a highly malignant human brain tumour, for which no cure is available at the present. The average survival after presentation with clinical symptoms from GBM is 1.5 years. The C6 cell glioma model is often used for experiments during the pre-clinical stage to test novel therapeutic approaches that might increase the recurrence-free survival time for human patients with GBM.

C6 is a commercially available tumour cell line, with the advantage that the tumour cells have been raised in rats and therefore no immunosuppression is required to allow implanted tumour cells to multiply in the brain of rats as host animals. A second advantage is that C6 gliomas exhibit characteristics equal or very similar to those found in human malignant glioma. Implanted glioma cells multiply in the rodent brain and form an irregularly shaped solid tumour of 2.5–4 mm within 2 weeks after implantation. If no therapy is given between weeks 2 and 3 after C6 cell implantation, the animals usually die as a consequence of increased intracranial pressure. Some of the tumour cells migrate to brain regions distant from the local tumour bulk [27].

The aim of the project was to (a) study the composition of healthy brain structures, (b) identify spectra characteristic for malignant brain tumours and (c) search for spectral changes caused by the presence of malignant tumours on the adjacent brain tissue.

2. Materials and methods

Two adult male Wistar rats were used for our studies. One rat served as host for a brain tumour and one rat was used as an age-matched healthy control. The animals were housed and cared for in a temperature-regulated animal facility exposed to a 12-h light/dark cycle in accordance with the guidelines of the Canadian Council on Animal Care. To generate the brain tumour, C6 cell cultures were expanded to confluence, harvested and stored in an ice bucket. Anaesthesia was achieved in the host animal with 5% Halothane® in oxygen with a flow rate of 1.5 l/min for induction and 2% Halothane® with the same oxygen flow rate for continuation of anaesthesia. A subcutaneous injection of 0.05 mg Buprenorphine®/kg was administered as premedication and served, considering the shortness of the surgical procedure, also the purpose of post-surgical analgesia. The head of the animal was shaved and disinfected with Hibitane® (chlorhexidine) and 70% alcohol. A straight parasagittal incision of skin and periosteum was performed about three mm to the right of the midline. A burr hole of 0.6 mm diameter was placed three mm behind the coronary suture. About 100,000 C6 cells were suspended in a total volume of 5 μl Hank's solution and loaded in a Hamilton syringe. To assure that the tumour cell injection caused a minimum of trauma to the brain, the Hamilton syringe was attached to a syringe pump (KDS 310, Geneq, Canada). The cells were injected over a period of 2 min into the anterior part of the right brain hemisphere of the anaesthetized animal. At the end of the injection procedure, the burr hole in the skull bone was closed with a plug of bone wax and the skin was sutured. The animal was allowed to recover. It was sacrificed 2 weeks after C6 cell implantation, at which time an irregularly shaped tumour mass had developed in the right cerebral hemisphere (diameters of 2.5–4 mm). Both animals were sacrificed under Halothane® anaesthesia by intracardiac perfusion with normal saline (1 ml/g rat) and 10% Formalin (1 ml/g rat). The brains were isolated, stored in 10% Formalin overnight and processed for embedding in paraffin. Coronal sections of 4 μm thickness were mounted alternately on either superfrost® slides (VWR) or IR reflecting slides (MIRR-IR, Kevley Technologies, OH, U.S.A.). The sections mounted on MIRR-IR slides were de-paraffinised in a xylene bath for 3 min and then air-dried. The xylene treatment presumably greatly reduces the phospholipid content of the tissue samples. While cryo-microtomed sections might offer spectroscopic information on lipid content that is largely lost through the paraffin embedding procedure it was thought that cryo-sectioning to 4 μm thickness would make the production of histologically presentable sections extremely difficult. Sections on the superfrost® slides were stained with Hematoxylin and Eosin (H&E).

IR spectra were acquired at the Centre for Biospectroscopy at Monash University in Melbourne, Australia, using a "Stingray" FTIR microscope system (Varian Inc.) equipped with a mercury cadmium telluride (MCT) 64×64 focal plane array (FPA). Spectra were recorded in reflection/absorption mode at 6 cm^{-1} resolution over the region 4000–900 cm^{-1}. The samples were imaged as 1024-tile (32×32) mosaics which covered an 11.26×11.26 mm area at a nominal pixel spatial resolution of 88 μm. The resulting FTIR images were processed using CytoSpec [28] spectroscopic software. The spectra contained in each image pixel were then subjected to a quality test and those pixels which passed were then further processed in CytoSpec to generate both chemical images (chem-images) and UHCA maps. Each of the chem-images plots image intensity as a function of the integrated area under a chosen spectral band after subtraction of the local baseline. By choosing to plot integrated band areas as opposed to absorbance at a single wavenumber the chem-images produced are less influenced by baseline effects and band shifts. The UHCA maps were produced using CytoSpec and the UHCA analysis was performed on the second derivatives of the spectra contained within the images. The UHCA was performed on the spectral region 1800–900 cm^{-1}, which includes the amide region (1700–1250 cm^{-1}), the ν_{as} PO_2^- region (1250–1200 cm^{-1}) and the ν_{as} C–O region (1060–1000 cm^{-1}). UHCA collects similar spectra into groups or clusters. The resulting false-colour cluster maps were directly compared with the H&E stained sections to assist in identifying both anatomical and histopathological features.

3. Results

3.1. Histology

H&E stained visible light micrographs of the healthy rat brain and a brain containing the malignant glioma are shown in Figs. 1a and b. In the micrograph of healthy brain various anatomical structures can be readily identified, such as, the cortex, the caudoputamen, the corpus callosum, the septal nucleus and the anterior commissure. Also easily identifiable are the myelinated fibres running perpendicular to the plane of the section through the caudoputamen, which give the region its characteristic spotted appearance. In the brain section of the tumour–bearing animal the primary tumour site within the caudoputamen is clearly visible in the right hemisphere, just below the corpus callosum. As a consequence of the tumour

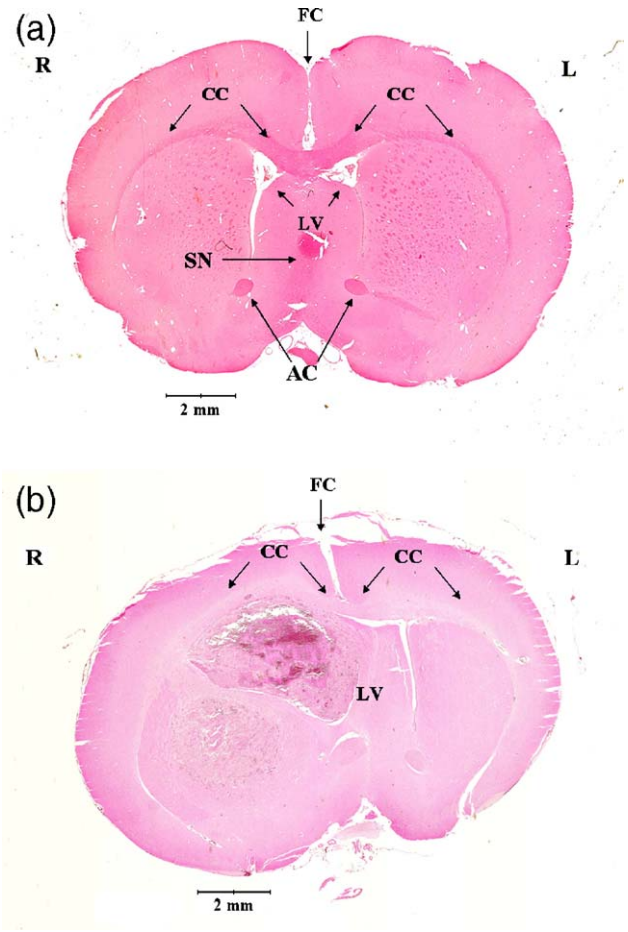

Fig. 1. Coronal sections of healthy rat brain (a) and brain with the malignant glioma (b). H&E stain, low magnification. FC: site of Falx cerebri (interhemispherical fissure), AC: anterior commissure, CC: corpus callosum; LV: lateral ventricle; SN: septal nucleus, R: right hemisphere; L: Left hemisphere.

growth, the brain morphology is distorted, the lateral ventricles have been compressed and midline-structures have been shifted towards the left. Infiltration of the tumour into the basal ganglia can be detected at low–medium magnification under the light microscope.

3.2. Protein region

The chem-images shown in Fig. 2 present the distribution of the amide I band (1700–1570 cm^{-1}) due to proteins within coronal sections of the healthy brain (a) and the brain containing the malignant glioma (b). All the chem-images presented here were produced by plotting final image intensity as proportional to the integrated area under the band of interest after subtraction of the local baseline. In the healthy brain the highest relative concentrations of proteins were found in the corpus callosum, and in various regions of the basal ganglia. The chem-image shows relatively low absorbance from amide I in most of the cortex. However, higher amide I absorbances were observed in an outer layer of the cortex, to a depth of approximately 300 μm. In the brain section of the tumour-bearing rat, the highest absorbances due to amide I were recorded at the site of the tumour. Interestingly, in the brain section of the tumour-bearing animal the corpus callosum showed lower absorbance at the amide I band compared to that in the cortex and the caudoputamen, in contrast to the result for the healthy brain.

3.3. Phosphodiester region

The chem-images in Fig. 3 present the absorbance distribution of the band at 1235 cm^{-1} mostly due to symmetric vibrations of phosphodiester groups of RNA and DNA. In the healthy brain sample the highest relative phosphodiester group absorbances were recorded in the medial region of the corpus callosum, in the commissure anterior and on a medial line through the basal ganglia. Intermediary absorbances were recorded for the lateral regions of the corpus callosum and within the caudoputamen. Most of the cortex appears to have the lowest relative phosphodiester absorbances. In the brain section of the tumour-bearing animal the highest phosphodiester absorbances were recorded in the tumour growth, with progressively lower absorbances in the cortex and the corpus callosum.

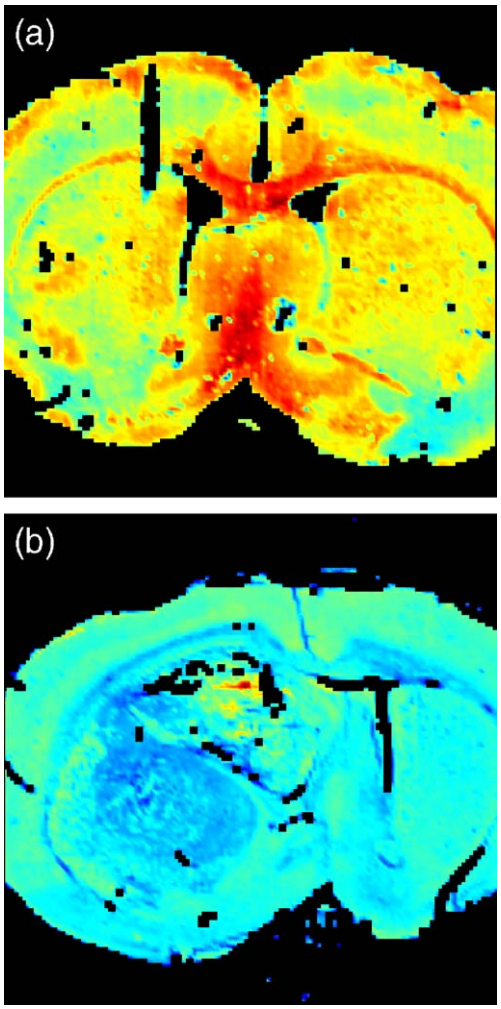

Fig. 2. Chem-images representing the distribution of amide I, (1620–1680 cm^{-1} integrated peak areas after baseline correction), in the healthy brain (a) and in the brain with the malignant glioma (b). Red indicates regions of highest absorbance and blue indicates regions of lowest absorbance.

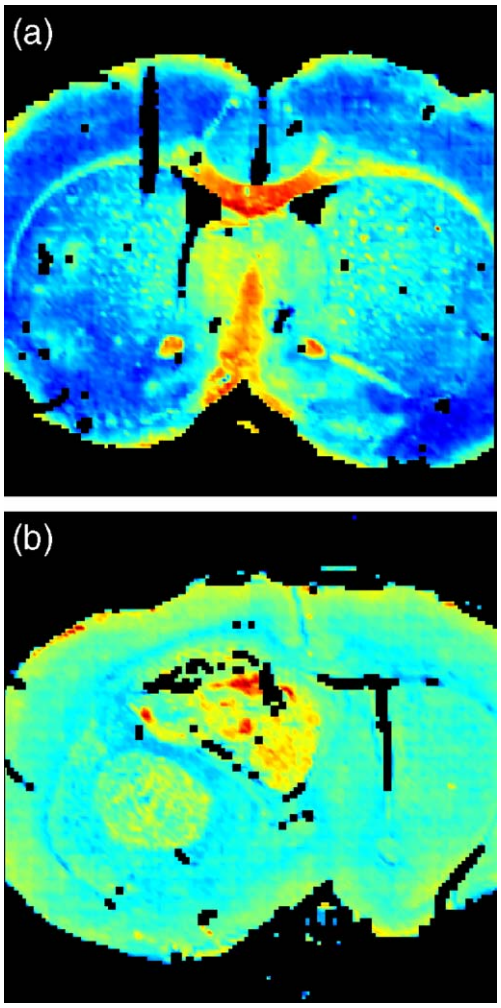

Fig. 3. Chem-images representing the distribution of phosphodiester, (1200–1270 cm^{-1} integrated peak areas after baseline correction), in the healthy brain (a) and in the brain with the malignant glioma (b). Red indicates regions of highest absorbance and blue indicates regions of lowest absorbance.

3.4. UHCA maps and representative spectra

Fig. 4 shows the cluster maps obtained when UHCA was performed on the healthy brain (a) and the brain containing the tumour (b) to produce just two clusters. For the two cluster UHCA of the healthy tissue section the white and grey matter areas are separately clustered. The two clusters UHCA of the tissue section of the tumour-bearing animal separated the tumour into one cluster and the non-tumorous tissue into the other.

Fig. 4c shows the four mean spectra obtained by averaging the collected spectra from each of the clusters. These four spectra are presented baseline corrected and vector normalised to remove absorbance variation that may be due solely to small differences in sample thickness of the two different tissue sections. The two spectra from the clusters in the healthy sample are very similar. However, the spectrum corresponding to the white matter exhibits slightly increased absorbance in the amide I and amide II bands from proteins and increased absorbance at the lower wavenumber end of the spectrum (particularly around the phosphodiester bands at 1235 and 1078 cm^{-1}) when compared to the spectrum corresponding to the grey matter. An increased absorbance at the lower wavenumber part of the spectra was also recorded for the two spectra obtained from the brain section of the tumour-bearing animal. The spectrum obtained from the cluster corresponding to the tumour exhibits a markedly decreased amide I/amide II ratio, a slight shift of the

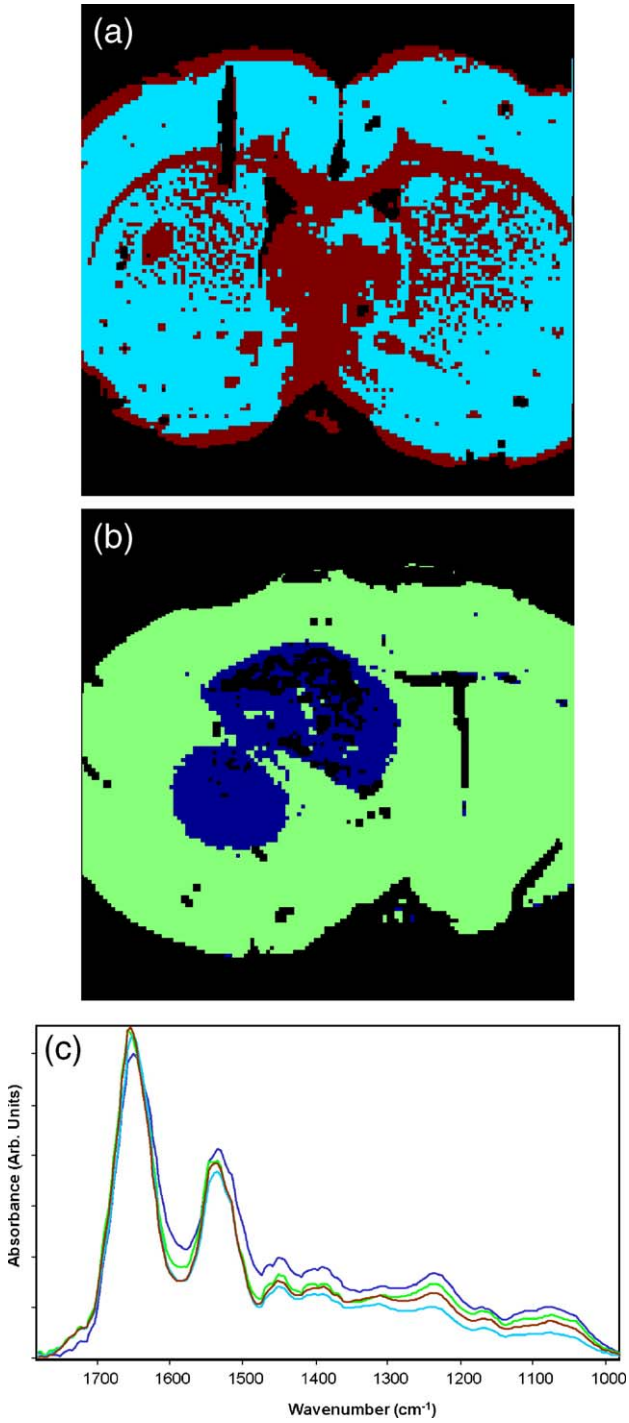

Fig. 4. UHCA maps generated for two clusters using the 900–1800 cm^{-1} spectral window, in the healthy brain (a) and in the brain with the malignant glioma (b). (c) Average cluster spectra from two cluster UHCA spectra colour coded to enable comparison with the cluster maps.

amide I peak towards lower wavenumber and a small absorbance increase in the bands due to phosphodiester vibrations.

Figs. 5a and b show the cluster maps obtained when UHCA was performed to produce maps containing eight clusters on the same tissue samples. At eight clusters many anatomical features can be identified in the healthy brain sample. Five layers are distinguishable in the cortex (yellow–orange–brown–green–brown) that may correspond to the outermost Brodmann layers. Three of the eight clusters (very-pale blue, red and yellow) corresponded to poor quality spectra that exhibited strong evidence of the dispersive artefact. This is not surprising as these cluster areas are located on the edge of the tissue sample and around holes in the tissue. The five remaining clusters correspond well with the tissue structures as follows; a cluster corresponding to the Brodmann layer IV in the cortex (green), a cluster containing an inner layer of the cortex and the grey matter areas in the caudoputamen (brown), a cluster for the white matter spots in the caudoputamen and most of the basal ganglia (orange), a cluster located in the lateral portions of the corpus callosum (light blue), and lastly, a cluster located at the medial portion of the corpus callosum, the commissure anterior and a medial spot in the basal ganglia (dark blue). The average spectra obtained from these five clusters have very similar profiles but changing total absorbance levels as can be seen in Fig. 5c.

The UHCA at eight clusters on the tumour sample spectra produced only three clusters that contained good quality spectra and corresponded with identifiable tissue structures. These three clusters were at locations corresponding to a large fraction of the tumour (pale green), the corpus callosum (pale blue) and most of the remainder of the non-tumorous fraction of the tissue section (brown). The average cluster spectra from these three clusters are shown in Fig. 5d. The spectrum from the caudoputamen differs from the spectrum of the remaining non-tumorous tissue fraction in that the caudoputamen spectrum exhibits reduced absorbance in the amide I and amide II protein bands. The tumour cluster spectrum has slightly increased absorbance at the lower wavenumber end of the spectrum when compared with the spectrum from the non-tumorous tissue fraction, particularly around the 1070 cm^{-1} band due to symmetric phosphodiester vibrations. The tumour cluster spectrum also exhibits a slight shift towards lower wavenumber and a slight broadening of the amide I band.

4. Discussion

The FTIR imaging and UHCA approach employed in this study was able to readily identify the tumour growth as chemically distinct from the surrounding brain tissue. The tumour and surrounding tissue were immediately separated at

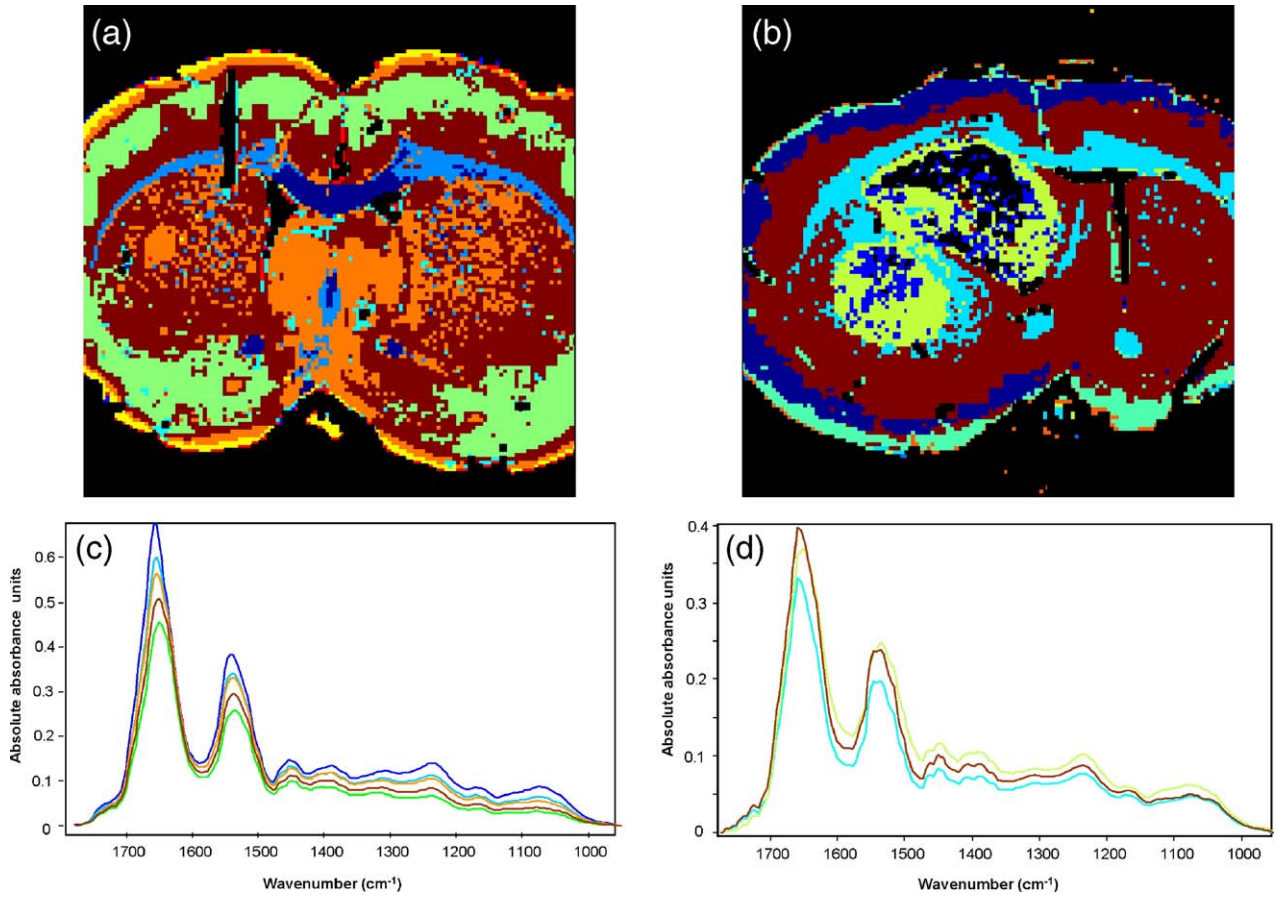

Fig. 5. UHCA maps generated for eight clusters using the 900–1800 cm^{-1} spectral window, in the healthy brain (a) and in the brain with the malignant glioma (b). Collected mean cluster spectra from eight cluster analyses, spectra colour coded to enable comparison with the cluster maps, for the healthy brain (c) and in the brain with the malignant glioma (d).

the first pair of clusters. In the FTIR chem-images and cluster maps the invasive portion of the tumour is clearly apparent, even more so than in the visible light micrographs.

UHCA of the FTIR images was also able to isolate and classify cluster average spectra for many of the brain structures present in the healthy brain tissue sample. These healthy tissue clusters showed very similar spectral profiles and varied mainly in total absorbance. The prominent bands observed included (a) amide I (~1650 cm^{-1}) and amide II (~1544 cm^{-1}) vibrations from proteins, (b) the acyl deformation modes from peptide side chains (~1460 cm^{-1}) (c) the COO^{-} stretching vibration at 1400 cm^{-1} mainly from amino acid side chains, (d) the asymmetric phosphodiester vibration around 1235 cm^{-1} from nucleic acids, (e) a band at around 1165 cm^{-1} due to symmetric C–O vibrations possibly originating from RNA and/or carbohydrates, and finally, (f) a broad spectral feature extending from 1030 to 1130 cm^{-1} most likely comprised of contributions from C–O stretching vibrations from ribose C–O skeletal vibrations in RNA and DNA and a strong contribution from the symmetric stretching vibration of phosphodiester groups in nucleic acids. Thus, the majority of the dominant bands in the spectra arise from proteins and nucleic acids. The changing total absorbance observed in the different cluster spectra obtained from the healthy brain tissue types might therefore be well explained as a simple measure of the ratio of proteins, DNA and ribosomal RNA versus the cellular cytoplasm fraction, with the highest IR absorption appearing in those tissue types with the greatest amount of protein content per unit tissue volume. It appears likely that the differing degrees of myelination present in the different brain structures is also being detected through its influence on the total protein content. The clustering in Fig. 4a shows distinction in regions with high myelin content (brown) versus regions with low myelin content (pale blue). The UHCA has distinguished between densely packed myelinated tracts (dark blue: corpus callosum and anterior commissure), morphologically less densely packed myelinated tracts (lighter blue: cingulum, external capsule and septal nucleus) and radiating myelinated fibres (orange in the caudoputamen and septal/fornix region).

The cluster analysis also appears to be identifying layers in the cortex, which correspond well with the six anatomical Brodmann layers of the neocortex. The Brodmann layers describe anatomical layers according to the cellularity, with higher and lower content of cell bodies. The cells of the outer cortical layer (layer I corresponding to the yellow cluster) have a low cytoplasmic/nuclear ratio. However, it is important to note that because of the proximity of this layer to the outer edge of the tissue other physical effects such as dispersion could also explain its separation from the more internal layers. Cell bodies with higher cytoplasmic/nuclear ratios are concentrated in layers II (orange), III, V and VI (brown). The third and fifth layers of the amide I chem-image (Fig 2a) show a similar amide I absorbance distribution; Brodmann layers III and V are both characterized by a high content of pyramidal cells (external and internal pyramidal layer). The relatively wide layer IV (green) corresponds to the internal granular layer, which contains only few neuronal bodies and is mostly composed of dendritic and axonal connections between cell bodies.

UHCA revealed spectral changes between the non-tumorous and the tumour tissues present in the section of the tumour-bearing animal. An increase in relative absorbance of most bands was observed for the tumour spectra that may be explained by an increase in the fractional content of proteins in the tumour cells compared to the unaffected cells. The tumour spectra also showed a slight decrease in the ratio of peaks heights from amide I/amide II, a shift in the amide I band toward lower wavenumber and a broadening of the amide I band. Recent articles [11,29,30] have described a dispersive artefact which can arise in reflection/absorption measurements and an artefact due to a Mie-type scattering mechanism, both of which can lead to non-Beer–Lambert absorption behaviour in infrared microspectroscopic observations of biological samples. It is not uncommon for the amide I band to be observed shifted towards lower wavenumber and reduced in height solely as a result of the dispersion artefact. Inspection of the spectral baselines showed little or no evidence of Mie-type scattering. However, at the edges of the tissue and within a few microns of holes in the tissue some distortion of the spectra was apparent, probably as a result of the dispersion artefact. To ensure that the integrated area of the amide I mode is representative of changes in protein concentration and not physical artefacts chem-images were produced that plotted image intensity as a function of the ratio of integrated, baseline corrected, amide I/amide II absorbances. The chem-images produced were found to be uniform and featureless across the vast majority of the tissue contained in the samples. As the total amide I/amide II absorbance was a constant throughout the majority of the sample we conclude that physical artefacts resulting in non-specific matrix type absorptions had little or no impact on the technique's ability to measure real changes in protein concentration based on the integrated intensity of the amide I mode. However, care must be taken when interpreting the shift observed in amide I band for the tumour spectra to ensure one is reporting a real chemical shift and not just a product of a physical artefact such as dispersion. The non-normalised mean extracted spectra presented in Fig. 5b appear to contain a mixture of different degrees of dispersion artefacts as they show a correlation between lower absorbance and red shifted wavenumber for the amide I mode, indicative of some physical effect contributing to the position of this band. Consequently, those cluster maps generated over the 1800–950 cm^{-1} range would appear to be based on spectral variation associated with physio-chemical differences as opposed to chemical differences alone. It would also appear that the major differences between clusters are based on variation associated with protein concentration and possible physical effects resulting in shifts in the amide I mode. Nonetheless, the cluster maps do show more detail and apparent information than the H&E stained sections. For instance it is clear from the cluster map presented in Fig. 4b that there is a narrow section of cells connecting the two tumorous masses together, which is not apparent in the visible image. Fig. 4c compares spectra collected from the tumour sample with spectra from the healthy sample. The spectra from the non-tumorous

fraction of the section from the tumour-bearing animal were observed to have increased absorbance around the phosphodiester bands compared to the spectra obtained from the healthy sample. At the eight clusters level several of the different tissue types present in the healthy sample were clearly separated by the UHCA, which was not the case for the tumour sample, where apart from the corpus callosum no tissue type differentiation was obtained from the UHCA. In the tumour sample the amide and phosphodiester absorbances in the corpus callosum were lower than for the corresponding bands in the surrounding tissue while for the healthy sample these two absorbance bands were stronger than in the other tissue types. Taken in combination these spectral changes indicate that FTIR imaging is capable of detecting physical–chemical differences from healthy tissue in the tumour sample at all points within the brain, not just at the site of the tumour growth itself.

It is interesting to note that in the eight cluster analysis the corpus callosum in the healthy sample was divided into two clusters, one cluster for the medial part and one cluster for the lateral zones. The site of the division of these clusters corresponds to the location of the feature known as the cingulum bundle.

UHCA is able to differentiate clusters based on spectral features that are sometimes extremely difficult to discern from the spectra by eye alone. For optimal results, the analysis of brain sections from healthy and tumour-bearing animals should be performed in the same data set. Unfortunately, that is not yet possible due to limitations in computer capacity. However, we have shown that FPA-based IR analysis of brain tissue in an animal model of malignant brain tumour can supply useful information with regard to the chemical composition of complex tissues that cannot be obtained otherwise.

Acknowledgements

We would like to thank Mehri Herman for dedicated animal care, Karen Yuen for preparation of the histological samples, Finlay Shanks for technical support with the Stingray instrument and Todd Reichert for his help in the photographic imaging suite.

This study was supported by the Saskatchewan Synchrotron Institute (SSI), the Brain Tumour Foundation of Canada, the National Health and Medical Research Council of Australia and an Australian Synchrotron Research Program Fellowship grant and a Monash University Synchrotron Fellowship.

References

[1] L. Chiriboga, P. Xie, V. Vigorita, D. Zarou, D. Zakim, M. Diem, Infrared spectroscopy of human tissue: II. A comparative study of spectra of biopsies of cervical squamous epithelium and of exfoliated cervical cells, Biospectroscopy 4 (1997) 55–59.

[2] B.R. Wood, K.R. Bambery, L.M. Miller, M.A. Quinn, L. Chiriboga, M. Diem, D. McNaughton, Infrared imaging of normal and diseased cervical tissue sections, Proc. SPIE 5651 (2005) 78–84.

[3] J.I. Chang, Y.B. Huang, P.C. Wu, C.C. Chen, S.C. Huang, Y.H. Tasaai, Characterization of human cervical precancerous tissue through the Fourier transform infrared microscopy with mapping method, Gynecol. Oncol. 91 (2003) 577–583.

[4] K.R. Bambery, B.R. Wood, M.A. Quinn, D. McNaughton, Fourier transform infrared imaging and unsupervised clustering applied to cervical biopsy, Aust. J. Chem. 57 (2004) 1139–1143.

[5] B.R. Wood, D. McNaughton, L. Chiriboga, H. Yee, M. Diem, Fourier transform infrared mapping of the cervical transformation zone, and dysplastic squamous epithelium, Gynecol. Oncol. 93 (2003) 59–68.

[6] Y. Fukuyama, S. Yoshida, S. Yanagisawa, M.A. Shimizu, A study on the differences between oral squamous cell carcinomas and normal oral mucosas measured by Fourier transform infrared spectroscopy, Biospectroscopy 5 (1999) 117–126.

[7] C.P. Schultz, K.Z. Liu, P.D. Kerr, H.H. Mantsch, In situ infrared histopathology of keratinization in human oral/oropharyngeal squamous cell carcinoma, Oncol. Res. 10 (1998) 277–286.

[8] L.M. MacIntosch, M. Jackson, H.H. Mantsch, M.F. Stranc, D. Pilavdzic, A. N. Crowson, Infrared spectra of basal cell carcinomas are distinct from non-tumour-bearing skin components, J. Invest. Dermatol. 112 (1999) 951–956.

[9] L.M. Macintosh, J.R. Mansfield, R. James, A.N. Crowson, H.H. Mantsch, Analysis and interpretation of infrared microscopic maps: visualisation and classification of skin components by digital staining and multivariate analysis, Biospectroscopy 5 (1999) 265–275.

[10] P.G.L. Andras, R.D. Strickland, Cancer grading by Fourier transform infrared spectroscopy, Biospectroscopy 4 (1998) 37–46.

[11] M.J. Romeo, M. Diem, Infrared spectral imaging of lymph nodes: strategies for analysis and artifact reduction, Vib. Spectrosc. 38 (2005) 115–119.

[12] P. Lasch, M. Diem, D. Naumann, FTIR microspectroscopic imaging of prostate tissue sections, Proc. SPIE 5321 (2004) 1–9.

[13] E. Gazi, J. Dwyer, P. Gardner, A. Ghanbari-Siahkali, A.P. Wade, J. Miyan, N.P. Lockyer, J.C. Vickerman, N.W. Clarke, J.H. Shanks, L.J. Scott, C.A. Hart, M. Brown, Applications of Fourier transform infrared microspectroscopy in studies of benign prostate and prostate cancer. A pilot study, J. Pathol. 201 (2003) 99–108.

[14] P. Lasch, W. Haensch, E.N. Lewis, L.H. Kidder, D. Naumann, Characterization of colorectal adenocarcinoma by spatially resolved FTIR microspectroscopy, Appl. Spectrosc. 56 (2002) 1–9.

[15] P. Lasch, W. Haensch, D. Naumann, M. Diem, Imaging of colorectal adenocarcinoma using FTIR microspectroscopy and cluster analysis, Biochim. Biophys. Acta 1688 (2004) 176–186.

[16] A. Salman, S. Argov, J. Ramesh, J. Goldstein, I. Simelnikov, H. Guterman, S. Mordechai, FTIR microscopic characterization of normal and malignant human colonic tissues, Cell Mol. Biol. 47 (2001) 159–166.

[17] K.C. McCrae, H.H. Mantsch, J.A. Thliveris, J.E. Scott, R.A. Shaw, Analysis in neoplastic changes in mouse lung using Fourier-transform infrared micro-spectroscopy, Vib. Spectrosc. 28 (2002) 189–197.

[18] L. Zhang, G.W. Small, A.S. Haka, L.H. Kidder, E.N. Lewis, Classification of Fourier transform infrared microspectroscopic imaging data of human breast cells by cluster analysis and artificial neural networks, Appl. Spectrosc. 57 (2003) 14–22.

[19] H. Fabian, P. Lasch, M. Boese, W. Haensch, Infrared microspectroscopic imaging of benign breast tumor tissue, J. Mol. Struct. 661–662 (2003) 411–417.

[20] L.-P. Choo, M. Jackson, W.C. Haliday, H.H. Mantsch, Infrared spectroscopic characterisation of multiple sclerosis plaques in the human central nervous system, Biochim. Biophys. Acta 1182 (1993) 333–337.

[21] H. Fabian, L.-P. Choo, G.I. Szendrei, M. Jackson, W.C. Halliday, L.J. Otvös, H.H. Mantsch, Infrared spectroscopic characterization of Alzheimer plaques, Appl. Spectrosc. 47 (1993) 1513–1518.

[22] J. Kneipp, P. Lasch, E. Baldauf, M. Beekes, D. Naumann, Detection of pathological molecular alterations in scapie-infected hamster brain by Fourier transform infrared (FTIR) spectroscopy, Biochim. Biophys. Acta 1501 (2000) 189–199.

[23] J. Dubois, R. Baydack, E. McKenzie, T. Booth, M. Jackson, Scrapie infection investigated by magnetic resonance imaging and Fourier transform infrared microscopy, Vib. Spectrosc. 32 (2003) 95–105.

[24] C. Beleites, G. Steiner, M.G. Sowa, R. Baumgartner, S. Sobottka, G. Schackert, R. Salzer, Classification of human gliomas by infrared imaging spectroscopy and chemometric image processing, Vib. Spectrosc. 38 (2005) 143–149.

[25] R. Wolthuis, M. van Aken, K. Fountas, J.S.J. Robinson, H.A. Bruining, G.J. Puppels, Determination of water concentration in brain tissue by Raman spectroscopy, Anal. Chem. 73 (2001) 3915–3920.
[26] R. Jyothi Lakshmi, V.B. Kartha, C. Murali Krishna, J.G.R. Solomon, G. Ullas, P. Uma Devie, Tissue Raman spectroscopy for the study of radiation damage: Brain irradiation of mice, Radiation Research 157 (2002) 175–182.
[27] X. Zhang, X. Li, J. Wu, Tissue Raman spectroscopy for the study of radiation damage: brain irradiation of mice, Zhonghua Yi Xue Za Zhi 81 (2001) 150–153.
[28] P. Lasch, A Matlab based application for infrared imaging see http://www.cytospec.com for details.
[29] M. Romeo, M. Diem, Correction of dispersive line shape artifact observed in diffuse reflection infrared spectroscopy and absorption/reflection (transflection) infrared micro-spectroscopy, Vib. Spectrosc. 38 (2005) 129–132.
[30] B. Mohlenhoff, M. Romeo, M. Diem, B.R. Wood, Mie-type scattering and non-Beer–Lambert absorption behavior of human cells in infrared microspectroscopy, Biophys. J. 88 (2005) 3635–3640.